NeuroImage 195 (2019) 454–462

Contents lists available at ScienceDirect

NeuroImage

journal homepage: www.elsevier.com/locate/neuroimage

Auditory white matter pathways are associated with effective connectivity of auditory prediction errors within a fronto-temporal network

Lena K.L. Oestreich [a,c,*], Roshini Randeniya [b,d], Marta I. Garrido [b,c,d,e]

[a] UQ Centre for Clinical Research, The University of Queensland, Brisbane, 4029, Australia
[b] Queensland Brain Institute, The University of Queensland, Brisbane, 4072, Australia
[c] Centre for Advanced Imaging, The University of Queensland, Brisbane, 4072, Australia
[d] Australian Centre of Excellence for Integrative Brain Function, Australia
[e] School of Mathematics and Physics, The University of Queensland, Brisbane, 4072, Australia

ARTICLE INFO

Keywords:
Auditory prediction error
Structural connectivity
Effective connectivity
Dynamic causal modelling (DCM)
Electroencephalography (EEG)
Diffusion magnetic resonance imaging (dMRI)

ABSTRACT

Auditory prediction errors, i.e. the mismatch between predicted, forthcoming auditory sensations and actual sensory input, trigger the detection of surprising auditory events in the environment. Auditory mismatches engage a hierarchical functional network of cortical sources, which are also interconnected by auditory white matter pathways. Hence it is plausible that these structural and functional networks are quantitatively related. The present study set out to investigate whether structural connectivity of auditory white matter pathways enables the effective connectivity underpinning auditory mismatch responses. Participants (N = 89) underwent diffusion weighted magnetic resonance imaging (MRI) and electroencephalographic (EEG) recordings. Anatomically-constrained tractography was used to extract auditory white matter pathways, namely the bilateral arcuate fasciculi, inferior fronto-occipital fasciculi (IFOF), and the auditory interhemispheric pathway, from which Apparent Fibre Density (AFD) was calculated. EEG data were recorded in the same participants during a stochastic oddball paradigm, which was used to elicit auditory prediction error responses. Dynamic causal modelling was used to investigate the effective connectivity underlying auditory mismatch responses generated in brain regions interconnected by the above mentioned auditory white matter pathways. Our results showed that brain areas interconnected by all auditory white matter pathways best explained the dynamics of auditory mismatch responses. Furthermore, AFD in the right arcuate fasciculus was significantly associated with the effective connectivity between the cortical regions that lie within it. Taken together, these findings indicate that auditory prediction errors recruit a fronto-temporal network of brain regions that are effectively and structurally connected by auditory white matter pathways.

1. Introduction

Auditory prediction errors are elicited by unexpected auditory events and result from a mismatch between predictions about forthcoming auditory sensations and actual auditory input (Friston, 2005). Previous studies used dynamic causal modelling (DCM) to investigate the effective connectivity of auditory mismatch responses and identified a three-level hierarchical network comprised of connections from bilateral primary auditory cortex (A1) to the planum temporale (PT), and from the PT to the right inferior frontal gyrus (IFG) (Garrido et al., 2007, 2008). This network included intrinsic (within source) connections in A1 and extrinsic (between-sources), forward and backward, connections between A1, PT and IFG. Interestingly, these effectively connected brain areas are also structurally connected via the auditory white matter pathways of the arcuate fasciculus, inferior fronto-occipital fasciculus (IFOF), and the auditory interhemispheric pathway. It is therefore possible that the generation of auditory mismatch responses is facilitated through dynamic interactions along these white matter tracts.

The arcuate fasciculus directly connects speech production areas in the IFG to auditory perception areas in the PT and also has shorter, indirect connections consisting of an anterior pathway which connects IFG to the inferior parietal lobule (IPL), and a posterior pathway which connects IPL to PT (Catani et al., 2005). While the posterior pathway has been reported to be involved in auditory comprehension, the anterior pathway is thought to be involved in the vocalization of semantic information (Catani et al., 2005). The IFOF connects areas in the frontal

* Corresponding author. UQ Centre for Clinical Research, The University of Queensland, Herston, QLD, 4029, Australia.
E-mail address: l.oestreich@uq.edu.au (L.K.L. Oestreich).

https://doi.org/10.1016/j.neuroimage.2019.04.008
Received 25 September 2018; Received in revised form 26 March 2019; Accepted 2 April 2019
Available online 5 April 2019
1053-8119/

lobe (including IFG) with temporal areas (including PT and A1) and occipital areas (Martino et al., 2010) and has been reported to be involved in semantic language processing (Duffau et al., 2005). The auditory interhemispheric pathway is part of the corpus callosum, linking bilateral A1s and PTs and is thought to be involved in the integration of prosodic and syntactic information (Wigand et al., 2015).

While it is generally accepted that white matter pathways serve as the structural basis for functional connectivity, a direct statistical relationship between the effective connectivity of mismatch responses and white matter microstructure is missing from the current literature and only few studies to date have attempted to directly associate measures derived from diffusion magnetic resonance imaging (MRI) with effective connectivity. Studies using DCM on fMRI data in combination with diffusion MRI reported correlations between measures derived from diffusion weighted imaging (DWI) and effective connectivity (Rae et al., 2015; Wagner et al., 2015). A study by Stephan et al. (2009) reported that DCMs informed by anatomical priors outperformed DCMs not informed by anatomical priors, which was taken to indicate that structural connectivity improves inferences about effective connectivity. Previous studies using diffusion MRI in combination with intracranial electrodes in patients with epilepsy also reported correlations between structural and effective connectivity (Conner et al., 2011; Donos et al., 2016). While these studies provide evidence for an association between effective and structural connectivity, they suffer from methodological limitations: fMRI has low temporal resolution and is therefore not suitable for inferences about fast sensory processing. Intracranial electrodes are invasive and can therefore only be used in samples of neurological patients. This makes it difficult to verify the results in larger samples of healthy individuals, which are required to make assumptions about healthy brain structure and function. To date, no studies have investigated whether structural connectivity derived from diffusion MRI facilitates effective connectivity inferred from non-invasive, scalp-derived electroencephalography (EEG), which, due to its higher temporal resolution, is better suited than fMRI to investigate whether structural connectivity enables fast brain dynamics, such as those underlying auditory change detection (which occurs approximately 100–200 ms after stimulus onset (Näätänen and Alho, 1997)).

In a previous study, we found that DCMs including brain regions hypothetically informed by auditory white matter pathways explained EEG responses to speech that is externally-generated, but temporally predictable (Oestreich et al., 2018). Here, we set out to directly quantify the statistical relationship between structural connectivity (from DWI) and effective connectivity from scalp-derived EEG data, with the aim of elucidating putative associations between auditory white matter pathways and effective connectivity between cortical regions defined along them, in the context of auditory mismatch responses. It was hypothesized that the effective connectivity network underlying auditory prediction errors would include connections along the auditory white matter pathways of the bilateral arcuate fasciculi, IFOF as well as the auditory interhemispheric pathway. It was furthermore hypothesized that the effective connectivity underlying auditory mismatch responses would be associated with structural connectivity of auditory white matter pathways.

2. Methods

2.1. Participants

Eighty-nine healthy participants (18–63 years, $M = 25.02$, $SD = 10.34$, 92.3% right-handed, and 57% female) were recruited through the online recruitment system - SONA and a weekly newsletter distributed to staff and alumni at the University of Queensland, Australia. To be included in the study, participants had to be at least 18 year of age and able to converse fluently in English in order to complete questionnaires and understand instructions during the behavioural tasks. Exclusion criteria were any diagnosis of psychiatric or neurological disorder, movement disorders or head injury with loss of consciousness. All participants gave written informed consent and were monetarily reimbursed for their time. The study was approved by the University of Queensland Research Ethics Committee.

2.2. Procedure

In the first part of the experiment, participants completed a set of questions about their demographic details. In the second part of the experiment, participants were seated in a quiet, dimly lit room, where they underwent electroencephalography (EEG) recording. The experimental design consisted of an auditory frequency oddball paradigm (Garrido et al., 2013) and a simultaneous N-back task (Sweet, 2011). Participants listened to a stream of sounds with log-frequencies sampled from two Gaussian distributions with equal means (500 Hz) and different standard deviations (narrow: $\sigma_n = 0.5$ octaves; broad: $\sigma_b = 1.5$ octaves). All tones were played with duration of 50 ms, including 10 ms smooth rise and fall periods and inter-stimulus intervals of 500 ms. 10% of the tones were defined as standard tones, which were played at 500 Hz, i.e. at the mean of both distributions, and 10% of the tones were defined as deviant tones, which were played at 2000 Hz, i.e. at the tails of the distributions and hence outliers. Standard and deviant tones were inserted into the sound stream pseudo-randomly with the Gaussian contributing 80% of the tones. Participants were told to disregard the tones and to focus on the visual N-back task, in which they were instructed to press a button every time they saw the same letter was played 2 trials beforehand. The timings of the sounds and the visual N-back task were independent of each other in order to avoid motor and attention artefacts. The overall experiment lasted approximately 30 min and was divided into 4 blocks. The narrow and broad distribution conditions were presented in separate blocks and the order of the blocks was counter-balanced across participants. Participants returned 1–4 days later for the third part of the experiment, for which they underwent diffusion-weighted and T1-weighted magnetic resonance imaging (MRI).

2.3. Data acquisition and pre-processing

2.3.1. Electroencephalography (EEG)

Continuous EEG was recorded with a 64 Ag/AgCl BioSemi ActiView system at a sampling rate of 1024 Hz. External electrodes were placed on the outer canthi of both eyes, below and above the left eye and on both mastoids. Pre-processing and data analysis were performed using SPM12 (revision number: 6906; Wellcome Trust Centre for Neuroimaging, London; http://www.fil.ion.ucl.ac.uk/spm/) with MATLAB (MathWorks). Data were referenced to the common average reference and high-pass filtered above 0.5 Hz. Ocular artefacts were detected and corrected with topography-based correction (Berg and Scherg, 1994). The data were epoched offline into 500 ms intervals with 100 ms pre- and 400 ms post-stimulus onset. Trials containing artefacts exceeding ±50 μV were rejected. Approximately 93% of trials survived the rejection procedure. The remaining artefact free trials were robustly averaged to event-related potentials (ERPs), low-pass filtered below 40 Hz and baseline corrected using the −100 to 0 ms pre-stimulus interval.

2.3.2. Source reconstruction and analysis

Source images were created from the scalp activity using a Boundary Element Method (BEM) and coregistered to individual head meshes based on each participant's structural T1 scans (as implemented in SPM 12). The resulting forward model was inverted within a Parametric Empirical Bayesian (PEB) framework using a Multiple Sparse Priors (MSP) approach for the variance components under group constraints (Friston et al., 2008b), which allowed for inferences about sensor-level data generated by the most likely cortical regions. The Greedy Search fitting algorithm was used for optimizing the MSP approach (Friston et al., 2008a). Reconstructed images were obtained in 0–400 ms time

intervals for the 4 conditions *Standard Narrow* (standard tones sampled from a Gaussian distribution of 500 Hz ± .5 octaves), *Deviant Narrow* (deviant tones defined as outliers to Gaussian distribution of 500 Hz ± .5 octaves), *Standard Broad* (standard tones sampled from a Gaussian distribution of 500 Hz ± 1.5 octaves) and *Deviant Broad Narrow* (deviant tones defined as outliers to Gaussian distribution of 500 Hz ± 1.5 octaves) for each participant and smoothed at FWHM $8 \times 8 \times 8$ mm^3. A mixed analysis of variance (ANOVA) was conducted with the within-subjects factors *surprise* (standards/deviants) and *variance* (narrow/broad) and significant main effects and interactions were followed-up with t-statistic contrasts. Brain regions identified in the source analysis were used to inform the nodes/brain regions of the DCMs in addition to auditory white matter pathways. It should be acknowledged that BEM and source estimates do not account for structural connectivity as these methods rely on Maxwell's equations (no conduction delays) and assume isotropy. On the other hand, DCM and DWI rely on a different set of assumptions such as anisotropy and limitations on propagation speeds. However, source reconstruction was merely used here for the purposes of informing our DCMs about cortical regsion likely to be elicited in this process.

2.3.3. Dynamic causal modelling (DCM)

DCM is based on a generative spatiotemporal model for EEG responses elicited by experimental stimuli (Kiebel et al., 2008). It uses neural mass models to make inferences about source activation as well as the dynamic interactions, or connectivity, amongst these sources (David and Friston, 2003; Jansen and Rit, 1995). In DCM, nodes are hierarchically organized and interconnected via forward, backward and lateral connections (David et al., 2005; Felleman and Van Essen, 1991; Kiebel et al., 2007). DCMs are defined to test theoretically informed hypotheses about several connectivity models which define alternative networks that explain (or predict) the generation of ERP signals (Garrido et al., 2008).

2.3.4. Bayesian model selection and averaging

Bayesian Model Selection (BMS) was used to compare several plausible network connections by estimating the probability of the data given a particular model within the space of models compared (Penny et al., 2004). In DCM, models with a high accuracy and low complexity have the highest evidence. A model with a poorer fit can have more evidence than a model with a good fit, if it is more generalizable (Friston et al., 2013). In other words, if there is a lot of measurement noise, a good model should identify this as noise rather than signal. In this case, the model will be better than a model that tries to fit noisy fluctuations (Friston et al., 2013; Breakspear, 2013). The winning model is therefore the one, which displays the best balance between accuracy maximisation and complexity minimization.

The posterior probability of each model was calculated over all participants using a random effects approach (RFX; Stephan et al., 2009), which quantifies the probability that a particular model generated the data for any randomly chosen participant. The reported exceedance probability is the probability that one model is more likely than any other model, given the group data (Stephan et al., 2010). The main conclusions of the family comparisons are based on inferences with RFX exceedance probabilities of .89 on average (ranging from .78 to 1). The Bayesian omnibus risk (BOR) directly measures the probability that all model frequencies are indistinguishable, which quantifies the risk incurred when performing Bayesian model selection (Rigoux et al., 2014). The BOR is defined by a value between 0 and 1, whereby a value close to 1 indicates that the models are indistinguishable and a value close to 0 indicates that the models are well distinguishable from each other. In order to make inferences on individual connections, we used random-effects Bayesian Model Averaging (BMA) which computes a weighted average estimate of the individual connections across all models and participants, such that each model contributes to the overall estimate according to its posterior probability (Stephan et al., 2009).

2.3.5. DCM specification

The models compared in the present study include up to 10 bilateral brain regions, which were hierarchically organized into four levels. These alternative models were motivated by brain regions, which have previously been shown to be implicated in auditory prediction error generation (Garrido et al., 2013), were identified by the source reconstruction of the present data, and are interconnected by the auditory white matter pathways of the arcuate fasciculus, the auditory interhemispheric pathway and the inferior fronto-occipital fasciculus (IFOF). The bilateral primary auditory cortex (A1) was defined as the input node of auditory information. The arcuate fasciculus comprises a direct pathway between planum temporale (PT) and inferior frontal gyrus (IFG) as well as two indirect pathways, namely the anterior pathway, which connects inferior parietal lobule (IPL) to IFG and the posterior pathway, which connects PT to IPL. The IFOF interconnects IFG with PT and the occipital lobe (OL). Lastly, the auditory interhemispheric pathway connects A1 to PT in the left hemisphere to PT and A1 in the right hemisphere. The coordinates were chosen based on previous studies on MMN generation for STG, IFG (Opitz et al., 2002) and A1 (Rademacher et al., 2001) and language processing for IPL (Bitan et al., 2005) and PT (Osnes et al., 2011). The mean locations for the nodes were based on the MNI coordinates for left A1 (−52, −19, 7), right A1 (50, −21, 7), left PT (−57, −20, 1), right PT (54, −19, 1), left IPL (−53, −32, 33), right IPL (51, −33, 34), left IFG (−48, 13, 17), right IFG (49, 12, 17), left OL (−45, −75, 11) and right OL (44, −75, 5; see Fig. 1 (Lacadie et al., 2008)).

A model space of 50 models was considered, including symmetric and non-symmetric hierarchical models, with (models 1–25) and without (models 25–50) interhemispheric connections between the left and right A1 and PT, with and without indirect connections between PT and IFG via IPL as well as models with and without connections to OL (for a full description of the model space see Fig. 1 – note that 25 model architectures are displayed, which were tested with and without interhemispheric connections). All models included modulations of intrinsic connectivity at the level of A1 and were individually estimated and compared to each other using BMS. To investigate whether auditory prediction errors operate along interhemispheric connections in addition to unilateral connections, a family including all models with interhemispheric connections (i.e. *lateral connections* family) was compared to a family without interhemispheric connections (i.e. *no lateral connections* family). Lastly, to investigate whether connections along individual white matter tracts or a combination of all tracts were more likely to be utilized during auditory prediction error generation, the models were partitioned into four different families, namely the *auditory interhemispheric pathway* family, the *IFOF* family, the *arcuate fasciculus* family, and the *auditory interhemispheric pathway* + *IFOF* + *arcuate fasciculus* family (see Fig. 1). Each of the 50 models was fitted to every participant's mean ERP response in the time window of 0–400 ms after stimulus onset. The *Standard Narrow* condition elicited the lowest ERP amplitude in the MMN time window (100–200 ms after stimulus onset) and was given the lowest parametric weight (weight = 0), followed by increasing ERP amplitudes in the *Standard Broad* (weight = 1), *Deviant Broad* (weight = 2), and *Deviant Narrow* (weight = 3) conditions (see Fig. 2A).

2.3.6. Diffusion-weighted imaging (DWI)

Magnetic resonance imaging (MRI) was performed on a Siemens Trio 3T system (Erlangen, Germany), which was monitored and reviewed by experienced radiographers, who repeated all scans that showed excessive head movements. Two DWI series were acquired using an echo-planar imaging (EPI) sequence. The first DWI series consisted of a high *b*-value data set with field-of-view (FoV) of 220 mm, phase partial Fourier (PPF) 6/8, parallel acceleration factor 2, 55 slices, 2 mm isotropic resolution, 64 diffusion-sensitization directions at $b = 3000$ s/mm^2 with two $b = 0$, TR = 8600 ms, TE = 116 ms, and 10min acquisition time. The second DWI series consisted of a low *b*-value data set with FoV 220 mm, PPF 6/8, parallel acceleration factor 2, 55 slices, 2 mm isotropic resolution, 32 diffusion-sensitization directions at $b = 1000$ s/mm^2 with one

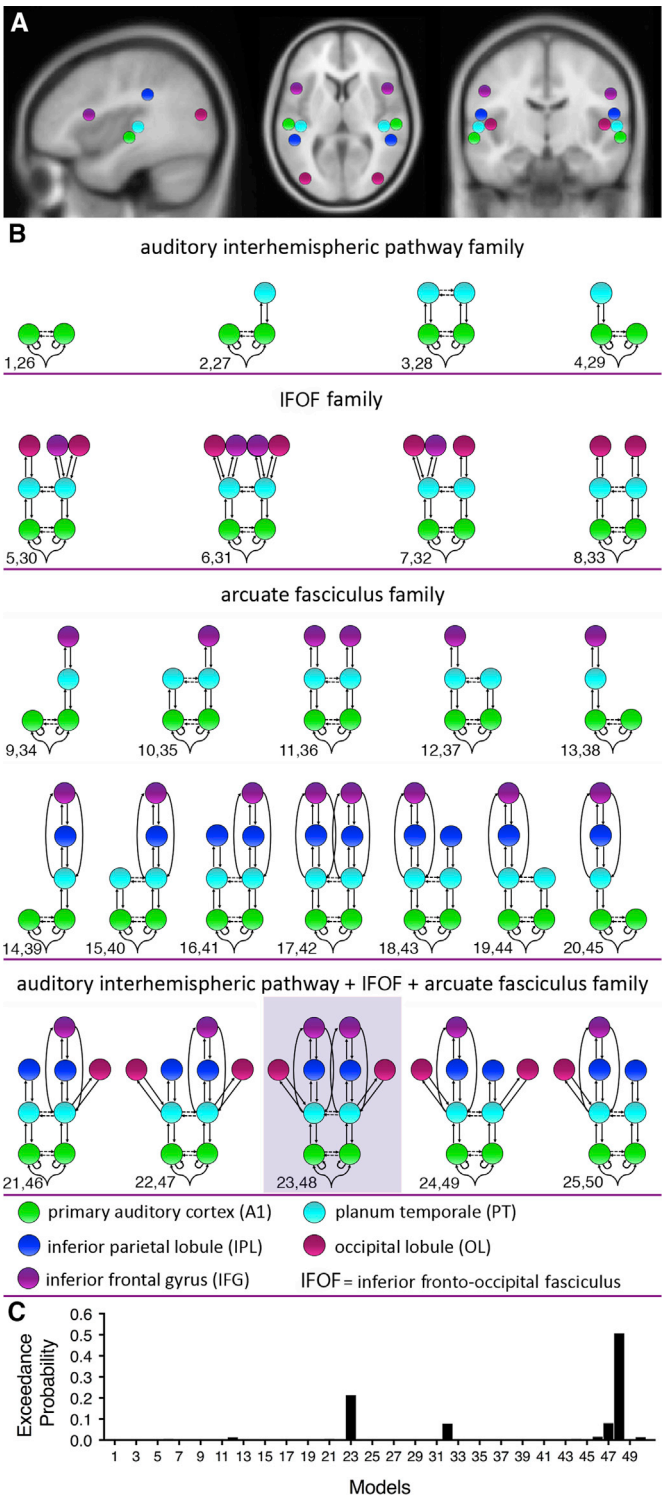

Fig. 1. A) Prior mean locations for the DCM nodes and model space. The MNI coordinates for the prior mean node locations included: left A1 (−52, −19, 7), right A1 (50, −21, 7), left PT (−57, −20, 1), right PT (54, −19, 1), left IPL (−53, −32, 33), right IPL (51, −33, 34), left IFG (−48, 13, 17), right IFG (49, 12, 17), left OL (−45, −75, 11) and right OL (44, −75, 5). B) Model space. Models 1–25 excluded interhemispheric connections between the A1s and PTs and models 26–50 included interhemispheric connections between the A1s and PTs. These 50 models were defined to test different hypotheses about the effective anatomy of auditory prediction error generation. The models were combined into 4 families including the *auditory interhemispheric pathway* family (models 1–4 and 26–29), the *IFOF* family (models 5–8 and 30–33), the *arcuate fasciculus* family (models 9–20 and 34–45), and *the auditory interhemispheric pathway + IFOF + arcuate fasciculus* family (models 21–25 and 46–50). C) Model exceedance probability for auditory prediction error generation. Bayesian model selection (random effects) over the whole model space indicated that auditory prediction error generation was best explained by model number 48 (highlighted by purple shading).

(caption on next column)

$b = 0$, TR = 8600 ms, TE = 116 ms, and 5min acquisition time. A T1-weighted image data set was acquired with the magnetisation-prepared two rapid acquisition gradient echo (MP2RAGE) sequence (Marques et al., 2010) with FoV 240 mm, 176 slices, 0.9 mm isotropic resolution, TR = 4000 ms, TE = 2.92 ms, TI1 = 700 ms, TI2 = 2220 ms, first flip angle = 6°, second flip angle = 7°, and 5min acquisition time. Three $b = 0$ images were acquired interspersed between the DWI series and the MP2RAGE sequence, with reversal of the acquisition direction along the phase-encoded axis for one of the three images and acquisition time of 30 ms each.

DWI scanc were corrected for signal intensity inhomogeneities (Zhang et al., 2001) as well as head movements and eddy current distortions using the FSL (version 5.0.11 FMRIB Software Library) TOPUP (Smith et al., 2004) and EDDY (Andersson and Sotiropoulos, 2016) tools. The remaining processing steps were conducted using tools implemented in MRtrix3 (version 0.3.16; Tournier et al., 2012). DW and T1-weighted images were co-registered using boundary-based registration (Greve and Fischl, 2009). A five-tissue-type segmented image (cortical grey matter, sub-cortical grey matter, white matter, cerebrospinal fluid, pathological tissue) was generated from the structural images pre-processed using the recon-all command in FeeSurfer (Stable v6.0; Dale et al., 1999). Response functions were estimated using the multi-shell, multi-tissue algorithm implemented in MRtrix3 (Jeurissen et al., 2014). Multi-tissue constrained spherical deconvolution was applied to obtain fiber orientation distributions (FOD; Jeurissen et al., 2014). Regions of interest (ROIs) were first drawn in Montreal neurological institute (MNI) space and then warped into individual subject space. ROIs for the auditory interhemispheric pathway were drawn in the primary auditory cortex (A1) and planum temporale (PT). The inferior fronto-occipital fasciculus (IFOF) was traced with ROIs placed in the inferior frontal gyrus (IFG), PT and occipital lobe (OL) and ROIs for the arcuate fasciculus were drawn in the PT, inferior parietal lobule (IPL) and IFG. All ROIs were defined separately in both hemispheres. ROIs were adjusted in individual subject space if necessary. For the IFOF and arcuate fasciculus, exclusion ROIs were drawn in the midline sagittal plane to exclude interhemispheric projections. Further exclusion ROIs were drawn to exclude any outlier tracts that were not consistent with the known anatomy of the respective pathways of interest. Anatomically-constrained tractography (ACT; Smith et al., 2012) was used to generate probabilistic streamlines of the auditory interhemispheric pathway, bilateral IFOF, and bilateral arcuate fasciculi with a maximum path length of 200 mm, a minimum path length of 4 mm, step size of 1 mm and back-tracking (see Fig. 3A). Spherical deconvolution Informed Filtering of Tractograms (SIFT2) is a filtering algorithm to remove inadequacies resulting from the reconstruction method to create tracts that are more biologically plausible (Smith et al., 2013). SIFT2 provides a cross-sectional area multiplier for each streamline, such that the contribution of each streamline to the tractogram can be weighted, whilst simultaneously retaining all reconstructed streamlines (Smith et al., 2015). Contrary to the traditional diffusion tensor model, which estimates average values across an entire voxel, the apparent fibre density (AFD) is a metric derived from the FOD lobe parallel to the direction of the streamline and therefore provides a sub-voxel, tract specific measure (Raffelt et al., 2012). The AFD integral for a FOD lobe in a specific direction is approximately proportional to the intra-axonal volume of the corresponding white matter fibre bundle oriented in that direction. AFD can therefore be defined as the fraction of space occupied

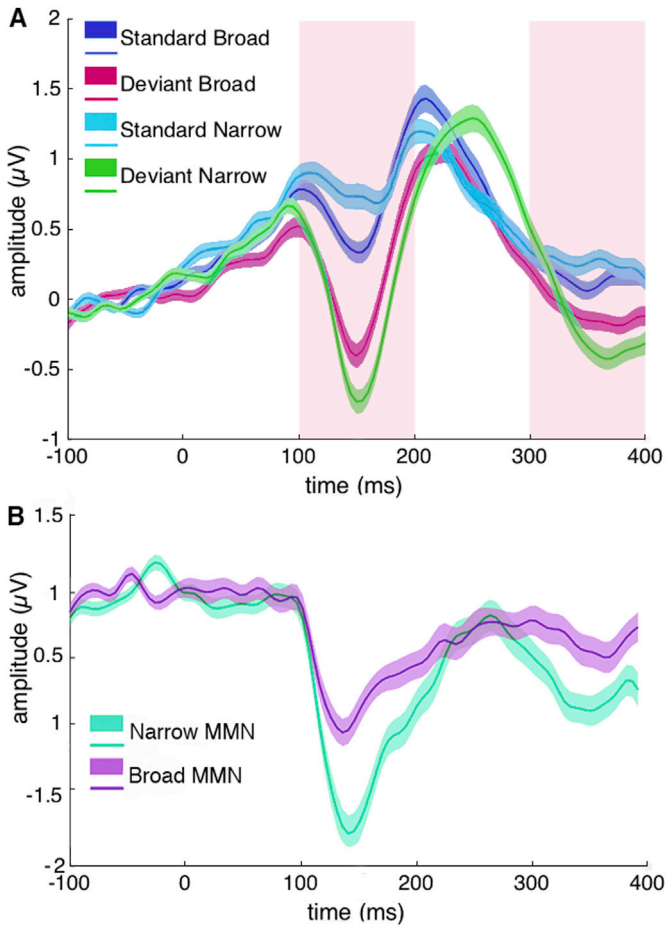

Fig. 2. Event-related potentials (ERPs) elicited by A) the *Standard Narrow* (light blue), *Standard Broad* (dark blue), *Deviant Broad* (magenta), and *Deviant Narrow* (green) conditions and B) mismatch negativity (MMN) waveforms (difference between responses to deviant and standard tones) for the broad (purple) and narrow (cyan) conditions extracted from electrode Fz. ERPs are time-locked to the onset of tones. Solid lines indicate the mean and lighter shading indicates standard error of the mean. MMN time window (100 ms–200 ms) and P300 time window (300 ms–400 ms) highlighted by pink shading.

by a white matter fibre bundle (Wright et al., 2017). The apparent fibre density (AFD) related to the total intra-axonal tract volume was calculated by summing the integrals for all FODs associated with the tract streamlines and dividing it by the streamline length (Raffelt et al., 2012).

2.3.7. Association between effective and structural connectivity

A multivariate normal regression implemented in Matlab using the function mvnrmle (Little and Rubin, 2002; Meng and Rubin, 1993), was fit to the DCM connectivity parameters derived from the BMA (i.e. the effective connectivity strength within- and between-sources calculated from the weighted average estimate of the individual connections across all models and participants - 26 outcome variables: intrinsic connections within left and right A1, interhemispheric connections between left and right A1, and left and right STG; reciprocal - forward and backward - connections linking A1 and PT, PT and IPL, IPL and IFG, PT and IFG, as well as PT and OL) where the effect of AFD was tested (5 independent variables: AFD of the right arcuate fasciculus, left arcuate fasciculus, right IFOF, left IFOF and the auditory interhemispheric pathway).

Next, we explored the specific associations between each individual white matter pathway and the effective connectivity between the cortical regions that lie within it. To this end we conducted five separate multiple regression analyses with AFD of the individual pathways as the outcome variable and the corresponding DCM connectivity parameters defined along those pathways as the independent variables. Bonferroni corrections were used to correct for multiple comparisons (i.e. p-value/5). In the first regression analysis, AFD of the right IFOF was entered as the outcome variable and the DCM connectivity parameters defined along the right IFOF as the independent variables (i.e., PT to IFG, IFG to PT, PT to OL, and OL to PT in the right hemisphere). In the second regression analysis, AFD of the left IFOF was entered as the outcome variable and the DCM connectivity parameters defined along it as the independent variables (i.e., PT to IFG, IFG to PT, PT to OL, and OL to PT in the left hemisphere). The third regression analysis was defined with AFD of the right arcuate fasciculus as the outcome variable and the DCM connectivity parameters defined along it as the independent variables (i.e., PT to IFG, IFG to PT, PT to IPL, IPL to PT, IPL to IFG, IFG to IPL in the right hemisphere). The fourth regression analysis was defined with AFD of the left arcuate fasciculus as the outcome variable and the DCM connectivity parameters defined along the left arcuate fasciculus as the independent variables (i.e., PT to IFG, IFG to PT, PT to IPL, IPL to PT, IPL to IFG, IFG to IPL in the left hemisphere). In the fifth regression analysis, AFD of the auditory interhemispheric pathway was entered as the outcome variable and the DCM connectivity parameters defined along it as the independent variables (i.e., left A1 to right A1, left W to right W, A1 to W in the left and right hemispheres as well as W to A1 in the left and right hemispheres).

3. Results

The event-related potential (ERP) waveforms of the prediction error responses, derived by subtracting the standards from the deviants, are displayed for the broad and narrow conditions in Fig. 2B. Summary statistics of the ERP waveforms are provided in the Supplement (Table S1).

3.1. Source level

Putative EEG sources were reconstructed from the scalp activity in order to infer the cortical sources most likely to have generated the observed EEG signal. A main effect of *surprise* was observed across bilateral temporal regions (see Table 1). A *surprise*variance* interaction was observed across occipital and parietal regions (see Table 1). These source activations are in line with previous findings in fMRI and EEG studies using MMN paradigms (Doeller et al., 2003; Garrido et al., 2013) which are also interconnected by auditory white matter pathways (see Fig. 3A) and therefore further support the selection of DCMs in the present study.

3.2. DCM analysis

In a first step, all 50 models with (models 1–25) and without (models 25–50) interhemispheric connections between bilateral A1 and PT were individually compared to each other. Results indicated that the best model included bilateral forward and backward connections between A1 and PT, PT and IPL, PT and OL, IPL and IFG, direct connections between PT and IFG as well as interhemispheric connections between left and right A1 and left and right PT (exceedance probability = .51; BOR = 9×10^{-6}; see Fig. 1B and C and Fig. S1 in the Supplement for mean and standard deviations of the effective connectivity strengths between connections in the winning model).

In order to investigate whether auditory prediction errors engage interhemispheric connections in addition to unilateral connections, a family including all models with interhemispheric connections was compared to a family without interhemispheric connections. BMS revealed that the *lateral connections* family was more likely than the *no lateral connections* family (exceedance probability = .78).

To test for specific hypotheses as to whether connections along individual white matter pathways or a combination of connections along all pathways are more likely to underlying the generation of mismatch responses, the models were partitioned into four different families as

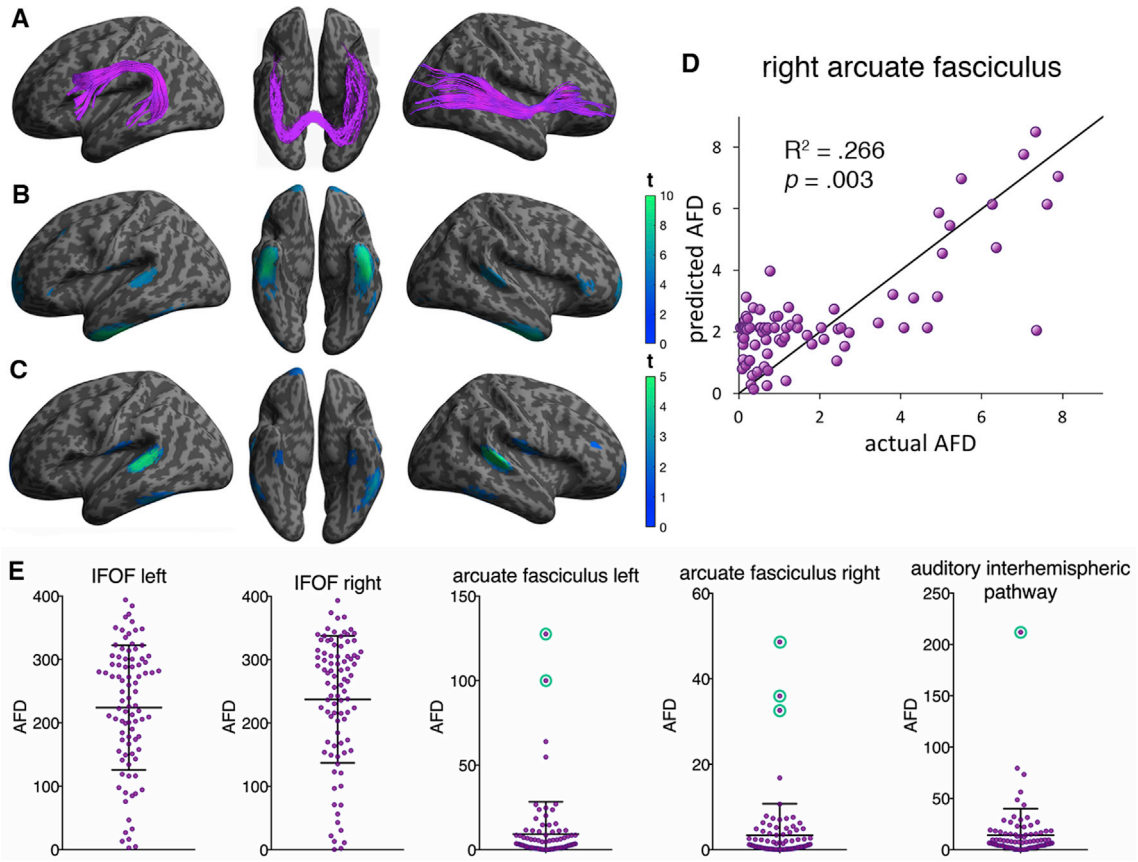

Fig. 3. A) Auditory white matter pathways warped onto an MNI template. The arcuate fasciculus connects IFG, IPL and PT (left), the auditory interhemispheric pathway connects bilateral A1 and PT (middle), and the inferior fronto-occipital fasciculus (IFOF) connects IFG, PT and OL (left). B) Source reconstructed images for the main effect of surprise (standards/deviants). All effects are displayed at an uncorrected threshold of $p < .05$ in the 0–400 ms time window. C) Source reconstructed images for the interaction between surprise and variance (narrow/broad). All effects are displayed at an uncorrected threshold of $p < .05$ in the 0–400 ms time window. D) Alignment between observed (actual) apparent fibre density (AFD) plotted against the predicted AFD (by the regression model, with DCM connectivity parameters PT to IFG, IFG to PT, IPL to IFG, IFG to IPL, PT to IPL, IPL to PT as predictor variables) of the right arcuate fasciculus. E) Apparent fibre density (AFD) of the five auditory white matter pathways. Error bars represent standard deviations (SD). Outliers defined as AFD > 3SD from the mean are highlighted in cyan and were excluded from analyses.

Table 1
Source analysis.

	coordinates			F-statistic (peak-level)	p-value	cluster size (voxels)
	mm	mm	mm			
main effect of *surprise*	−52	−20	−26	5.86	.016	81
	60	−26	−28	5.53	.019	47
surprise x variance interaction	38	−82	−16	2.85	.005	105
	−10	−24	74	1.73	.048	59

Note. All effects are displayed at an uncorrected threshold of $p < .05$.

described in the method section (see Fig. 1B). BMS of these families indicated that the *auditory interhemispheric + IFOF + arcuate fasciculus* family was the winning family (exceedance probability = .86), indicating that effective connectivity of auditory prediction errors is best explained by regions that are interconnected by all three auditory white matter pathways as opposed to one particular tract.

3.3. Association between effective and structural connectivity

Six statistical outliers (three in the right arcuate fasciculus, one in the auditory interhemispheric pathway and two in the left arcuate fasciculus; see Fig. 3E), defined as participants with AFD values greater than 3 standard deviations from the mean, were excluded from further analyses.

A multivariate normal regression was conducted in order to investigate whether the effective connectivity that underpins auditory mismatch responses could be predicted based on the structural connectivity of auditory white matter pathways. This was achieved by using the AFD values from the bilateral IFOF, arcuate fasciculi, and the auditory interhemispheric pathway as predictors and the twenty-six connectivity parameters derived with BMA over all DCMs as outcome variables. The structural connectivity of the right IFOF explained 5.2% (adjusted $R^2 = 0.052$ $p = .022$) and the right arcuate fasciculus explained 2.7% (adjusted $R^2 = 0.027$, $p = .049$) of the variance of the effective connectivity of the whole network (i.e. across all 26 connectivity parameters that were individually included as outcome variables in the regression analysis), indicating that effective connectivity underlying auditory mismatch responses increases with increasing structural connectivity (i.e. AFD) in the right IFOF and arcuate fasciculus. Detailed output of the regression analysis is provided in the Supplement (Table S2).

In order to explore specific associations between the auditory white matter tracts and the effective connectivity between the cortical sources that lie within them, we ran five independent multiple linear regressions, correcting the p-values with a Bonferroni correction for five comparisons. Only the AFD of the right arcuate fasciculus was significantly associated ($F = 4.586$, Bonferroni corrected $p = .003$) with the DCM connectivity parameters defined along the arcuate fasciculus (i.e. PT to IFG, IFG to PT, IPL to IFG, IFG to IPL, PT to IPL, IPL to PT). This indicates that the microstructure of the right arcuate fasciculus increases as the effective

connectivity between cortical regions interconnected by it increases. The overall model explained 27% of the variance of AFD of the right arcuate fasciculus (adjusted $R^2 = 0.266$; see Fig. 3D). Specifically, the AFD of the right arcuate fasciculus was trend-level associated with the forward connection from PT to IFG ($t = 1.949$, $p = .055$) and significantly associated with the forward connection from PT to IPL ($t = 2.518$, $p = .014$), the backward connection from IPL to PT ($t = -2.964$, $p = .004$), and the backward connection from IFG to IPL ($t = 2.33$, $p = .022$). None of the other regression analyses remained significant after correction for multiple comparisons. Detailed output of the regression analysis is provided in the Supplement (Table S3).

4. Discussion

The first aim of this study was to determine auditory white matter pathways that subserve the effective connectivity underpinning the generation of auditory mismatch responses. As hypothesized, the winning DCM model comprised brain regions interconnected by the bilateral arcuate fasciculi, bilateral IFOF and the auditory interhemispheric pathway. The second aim of this study was to investigate whether effective connectivity of auditory mismatch responses is associated with structural connectivity of auditory white matter pathways. We found that the white matter microstructure of the right IFOF and right arcuate fasciculus were significant predictors of the effective connectivity underlying mismatch responses. Moreover, greater effective connectivity between cortical regions interconnected by the arcuate fasciculus were significantly associated with increased white matter microstructure of the right arcuate fasciculus. Specifically, the backward connections from the inferior parietal lobule to the planum temporale, and the inferior frontal gyrus to the inferior parietal lobule, as well as the forward connections from planum temporale to inferior parietal lobule were individually associated with the microstructure of the right arcuate fasciculus. These findings indicate that auditory prediction errors are generated along a fronto-temporal auditory network that is both structurally and effectively connected.

In line with previous findings, the results of the present study indicate that auditory mismatches operate along hierarchically organized cortical brain regions including intrinsic connections and extrinsic forward and backward connections (Garrido et al., 2007, 2008). Specifically, the model that best explained auditory prediction error generation included intrinsic connections at A1, interhemispheric connections between bilateral A1s and PTs, as well as forward and backward connections between A1 and PT, PT and IPL, PT and IFG, PT and OL, and IPL and IFG. The present study refined previously employed models, which included recurrent connections between A1, PT and IFG, by including recurrent connections between PT and OL, PT and IPL, and IPL and IFG. These areas were added due to the fact that they are structurally interconnected by the auditory white matter pathways of the arcuate fasciculus, IFOF, and the auditory interhemispheric pathway. Furthermore, a previous study (Garrido et al., 2013) employed source reconstruction on MEG data using the same paradigm as used in the present study and found that the OL and IPL were engaged in auditory prediction error generation. It is therefore not surprising that the winning model of the present study outperforms those with a simpler architecture used in previous studies (Garrido et al., 2007, 2008).

The current study is one of the few studies to integrate structural neuroimaging measures with electrophysiological brain function measures (Deligianni et al., 2016; Fusar-Poli et al., 2011; Meier et al., 2016; Salisbury et al., 2007; Whitford et al., 2011; Wirsich et al., 2017) and, to the best of our knowledge, the first to integrate structural connectivity with effective connectivity from scalp-derived EEG data, within the same sample. We observed that the microstructure of the right IFOF and the right arcuate fasciculus significantly predicted the effective connectivity underlying auditory mismatch responses. Additionally, we found that the effective connectivity parameters along the right arcuate fasciculus accounted for a significant amount of variance (27%) of the right arcuate fasciculus microstructure. While the winning DCM model included brain areas along all auditory white matter pathways, the regression model did not suggest individual contributions of structural connectivity of the auditory interhemispheric pathway, the IFOF, or the arcuate fasciculus in the left hemisphere to be related to their associated effective connections. The interhemispheric pathway has mainly been associated with the integration of prosody and syntax (Wigand et al., 2015). The IFOF and the arcuate fasciculus on the other hand have been implicated in auditory and language processing more generally (Catani and Thiebaut de Schotten, 2008). The paradigm used in the present study consisted of simple tones rather than speech sounds and participants were passively listening to tones, instead of generating sounds themselves. It is therefore possible that even though the winning DCM model included areas along all of the auditory white matter tracts, areas interconnected by the IFOF and arcuate fasciculus play more critical roles in the generation of auditory mismatch responses than the auditory interhemispheric pathway.

In line with previous studies (Garrido et al., 2007, 2008), the current study also found that auditory prediction error generation is facilitated by an effective network of intrinsic connections within primary auditory cortex, forward and backward connections from bilateral primary auditory cortex to bilateral superior temporal gyrus (i.e. planum temporale). Contrary to previous studies however, which reported reciprocal connections from the superior temporal gyrus (i.e. planum temporale) to the inferior frontal gyrus (Garrido et al., 2007, 2008) in the right hemisphere only, we observed reciprocal connections from planum temporale to inferior frontal gyrus bilaterally. This could be explained by the fundamentally different and more complex nature of the stochastic oddball paradigm we used (Garrido et al., 2013), which might recruit more cortical sources. Nevertheless, we found that structural connectivity of the right arcuate fasciculus is associated with effective connectivity between cortical regions that lie within it. This supports previous findings of an auditory mismatch response network that is more prominent in the right hemisphere (Garrido et al., 2007, 2008).

Most effective connectivity parameters showed a positive association with the AFD values of the right arcuate fasciculus, such that effective connectivity increased with increasing structural connectivity. This indicates that the microstructure of the right arcuate fasciculus increases with increasing effective connectivity of auditory mismatch responses. However, the backward connection from inferior parietal lobule to planum temporale was negatively associated with the microstructure in the right arcuate fasciculus. This finding of decreased structural connectivity with increasing effective connectivity may seem counter intuitive. AFD is a measure of intra-axonal volume fraction (Raffelt et al., 2012), which can be interpreted such that high AFD values correspond to a high axonal density and low values indicate a reduction of axonal density. According to this interpretation, AFD values should increase with increasing effective connectivity, as opposed to decrease. One potential explanation for this finding is that since AFD is normalized by the total fibre length, participants with well-preserved longer-fibre communication and diverse branching might show decreased fibre density.

The ROIs used for tractography of the white matter pathways were first defined in MNI space to ensure the nodes from the DCM analysis were included. However, ROIs were then adjusted in individual subject space and differ in size to the nodes used in the DCM analysis. The fact that the ROIs used for tractography and DCM are not exactly the same therefore represents a limitation of this study and we cannot rule out the possibility that some fibres end slightly adjacent to the nodes used in the DCM analysis. Future studies may wish to include smaller ROIs for tractography and only reconstruct parts of white matter pathways that directly connect nodes included in the DCM analysis. Nevertheless, the nodes used in the DCM analysis only consider the coordinate of the peak activity (is agnostic to the shape of the cluster), and hence this should not have any implications for the demonstrated relationship between structural and functional connectivity underpinning mismatch responses. We reconstructed source images with a Boundary Element Method (BEM)

that identified brain areas likely to generate the electrical signal recorded on the scalp. BEM relies on Maxwell equations and assumes isotropy and therefore does not account for structural connectivity. However, it has to be noted that source reconstruction was solely used for the purpose of informing the prior mean locations of the DCM nodes and hence, the different sets of assumptions should not significantly impact the results of the study.

DCM studies in schizophrenia have reported reduced effective connectivity during auditory MMN generation (Dima et al., 2012; Ranlund et al., 2016) between the right IFG and PT (Dima et al., 2012), which are interconnected by the right arcuate fasciculus. Furthermore, MMN attenuation (Michie et al., 2016) and reduced microstructure in the arcuate fasciculus (Geoffroy et al., 2014) have consistently been reported in schizophrenia and have both been linked to auditory hallucinations (Fisher et al., 2012; McCarthy-Jones et al., 2015). To the extent that the structural connectivity of the right arcuate fasciculus was associated with effective connectivity between cortical regions that lie within it during auditory prediction error generation in the present study, future studies may wish to investigate whether the microstructure of the right arcuate fasciculus and effective connectivity of mismatch responses are indicative of auditory hallucinations prior to the development of florid psychosis.

While previous DCM studies have provided insights about the networks underpinning mismatch responses, it is important to note a couple of novel points unique to the present study, which are 1) its application to a novel paradigm (outliers vs. means in a sequence of sounds drawn from a Gaussian distribution) and 2) many different models not previously tested (including those with the occipital lobule and the inferior parietal lobule). In conclusion, we found that an effective network along the auditory white matter pathways of the bilateral arcuate fasciculi, bilateral IFOF and the auditory interhemispheric pathway best explained auditory mismatches in a statistical oddball paradigm. Critically, we observed, for the first time, that the structural connectivity (i.e. AFD) within the right arcuate fasciculus was significantly associated with the effective connectivity between brain regions that are interconnected by it. These auditory white matter pathways connect dynamically interacting brain regions and therefore provide a structural basis along which auditory mismatch responses are effectively generated in a stochastic environment.

Conflicts of interest

The authors have no conflicts of interest to declare.

Acknowledgements

This work was funded by the Australian Research Council Centre of Excellence for Integrative Brain Function (ARC Centre Grant CE140100007), a University of Queensland Fellowship (2016000071), and a Foundation Research Excellence Award (2016001844) to MIG, as well as a University of Queensland International Research Scholarship to RR. The authors thank the participants for their time and Aiman Al-Najjar and Nicole Atcheson for assisting with data collection.

Appendix A. Supplementary data

Supplementary data to this article can be found online at https://doi.org/10.1016/j.neuroimage.2019.04.008.

References

Andersson, J.L.R., Sotiropoulos, S.N., 2016. An integrated approach to correction for off-resonance effects and subject movement in diffusion MR imaging. Neuroimage 125, 1063–1078.
Berg, P., Scherg, M., 1994. A multiple source approach to the correction of eye artifacts. Electroencephalogr. Clin. Neurophysiol. 90, 229–241.
Bitan, T., Booth, J.R., Choy, J., Burman, D.D., Gitelman, D.R., Mesulam, M.M., 2005. Shifts of effective connectivity within a language network during rhyming and spelling. J. Neurosci. 25, 5397–5403.
Breakspear, M., 2013. Dynamic and stochastic models of neuroimaging data: a comment on Lohmann et al. Neuroimage 75, 270–274.
Catani, M., Jones, D.K., ffytche, D.H., 2005. Perisylvian language networks of the human brain. Ann. Neurol. 57, 8–16.
Catani, M., Thiebaut de Schotten, M., 2008. A diffusion tensor imaging tractography atlas for virtual in vivo dissections. Cortex 44, 1105–1132.
Conner, C.R., Ellmore, T.M., DiSano, M.A., Pieters, T.A., Potter, A.W., Tandon, N., 2011. Anatomic and electro-physiologic connectivity of the language system: a combined DTI-CCEP study. Comput. Biol. Med. 41, 1100–1109.
Dale, A.M., Fischl, B., Sereno, M.I., 1999. Cortical surface-based analysis. I. Segmentation and surface reconstruction. Neuroimage 9, 179–194.
David, O., Friston, K.J., 2003. A neural mass model for MEG/EEG: coupling and neuronal dynamics. Neuroimage 20, 1743–1755.
David, O., Harrison, L., Friston, K.J., 2005. Modelling event-related responses in the brain. Neuroimage 25, 756–770.
Deligianni, F., Carmichael, D.W., Zhang, G.H., Clark, C.A., Clayden, J.D., 2016. NODDI and tensor-based microstructural indices as predictors of functional connectivity. PLoS One 11, e0153404.
Dima, D., Frangou, S., Burge, L., Braeutigam, S., James, A.C., 2012. Abnormal intrinsic and extrinsic connectivity within the magnetic mismatch negativity brain network in schizophrenia: a preliminary study. Schizophr. Res. 135, 23–27.
Doeller, C.F., Opitz, B., Mecklinger, A., Krick, C., Reith, W., Schröger, E., 2003. Prefrontal cortex involvement in pre attentive auditory deviance detection:: neuroimaging and electrophysiological evidence. Neuroimage 20, 1270–1282.
Donos, C., Mălîia, M.D., Mîndruță, I., Popa, I., Ene, M., Bălănescu, B., Ciurea, A., Barborica, A., 2016. A connectomics approach combining structural and effective connectivity assessed by intracranial electrical stimulation. Neuroimage 132, 344–358.
Duffau, H., Gatignol, P., Mandonnet, E., Peruzzi, P., Tzourio-Mazoyer, N., Capelle, L., 2005. New insights into the anatomo-functional connectivity of the semantic system: a study using cortico-subcortical electrostimulations. Brain 128 (4), 797–810.
Felleman, D.J., Van Essen, D.C., 1991. Distributed hierarchical processing in the primate cerebral cortex. Cerebr. Cortex 1, 1–47.
Fisher, D.J., Labelle, A., Knott, V.J., 2012. Alterations of mismatch negativity (MMN) in schizophrenia patients with auditory hallucinations experiencing acute exacerbation of illness. Schizophr. Res. 139, 237–245.
Friston, K., Chu, C., Mourão-Miranda, J., Hulme, O., Rees, G., Penny, W., Ashburner, J., 2008a. Bayesian decoding of brain images. Neuroimage 39, 181–205.
Friston, K., Daunizeau, J., Stephan, K.E., 2013. Model selection and gobbledygook: response to Lohmann et al. Neuroimage 75, 275–278 discussion 279-281.
Friston, K., Harrison, L., Daunizeau, J., Kiebel, S., Phillips, C., Trujillo-Barreto, N., Henson, R., Flandin, G., Mattout, J., 2008b. Multiple sparse priors for the M/EEG inverse problem. Neuroimage 39, 1104–1120.
Friston, K.J., 2005. A theory of cortical responses. Phil. Trans. Roy. Soc. Lond. 360.
Fusar-Poli, P., Crossley, N., Woolley, J., Carletti, F., Perez-Iglesias, R., Broome, M., Johns, L., Tabraham, P., Bramon, E., McGuire, P., 2011. White matter alterations related to P300 abnormalities in individuals at high risk for psychosis: an MRI-EEG study. J. Psychiatry Neurosci. : JPN 36, 239–248.
Garrido, M.I., Friston, K.J., Kiebel, S.J., Stephan, K.E., Baldeweg, T., Kilner, J.M., 2008. The functional anatomy of the MMN: a DCM study of the roving paradigm. Neuroimage 42, 936–944.
Garrido, M.I., Kilner, J.M., Kiebel, S.J., Stephan, K.E., Friston, K.J., 2007. Dynamic causal modelling of evoked potentials: a reproducibility study. Neuroimage 36, 571–580.
Garrido, M.I., Sahani, M., Dolan, R.J., 2013. Outlier responses reflect sensitivity to statistical structure in the human brain. PLoS Comput. Biol. 9, 234–237.
Geoffroy, P.A., Houenou, J., Duhamel, A., Amad, A., De Weijer, A.D., Curčić-Blake, B., Linden, D.E., Thomas, P., Jardri, R., 2014. The arcuate fasciculus in auditory-verbal hallucinations: a meta analysis of diffusion-tensor-imaging studies. Schizophr. Res. 159, 234–237.
Greve, D.N., Fischl, B., 2009. Accurate and robust brain image alignment using boundary-based registration. Neuroimage 48, 63–72.
Jansen, B.H., Rit, V.G., 1995. Electroencephalogram and visual evoked potential generation in a mathematical model of coupled cortical columns. Biol. Cybern. 73, 357–366.
Jeurissen, B., Tournier, J.-D., Dhollander, T., Connelly, A., Sijbers, J., 2014. Multi-tissue constrained spherical deconvolution for improved analysis of multi-shell diffusion MRI data. Neuroimage 103, 411–426.
Kiebel, S.J., Garrido, M.I., Friston, K.J., 2007. Dynamic causal modelling of evoked responses: the role of intrinsic connections. Neuroimage 36, 332–345.
Kiebel, S.J., Garrido, M.I., Moran, R.J., Friston, K.J., 2008. Dynamic causal modelling for EEG and MEG. Cognitive Neurodynamics 2, 121–136.
Lacadie, C.M., Fulbright, R.K., Arora, J., Constable, R.T., Papademetris, X., 2008. Brodmann areas defined in MNI space using a new tracing tool in BioImage suite. In: Paper Presented at the Human Brain Mapping.
Little, R.J.A., Rubin, D.B., 2002. Statistical Analysis with Missing Data, 2 ed. John Wiley & Sons.
Marques, J.P., Kober, T., Krueger, G., van der Zwaag, W., Van de Moortele, P.-F., Gruetter, R., 2010. MP2RAGE, a self bias-field corrected sequence for improved segmentation and T1-mapping at high field. Neuroimage 49, 1271–1281.
Martino, J., Brogna, C., Robles, S.G., Vergani, F., Duffau, H., 2010. Anatomic dissection of the inferior fronto-occipital fasciculus revisited in the lights of brain stimulation data. Cortex 46, 691–699.

McCarthy-Jones, S., Oestreich, L.K.L., Bank, A.S.R., Whitford, T.J., 2015. Reduced integrity of the left arcuate fasciculus is specifically associated with hallucinations in the auditory verbal modality in schizophrenia. Schizophr. Res. 162, 1–6.
Meier, J., Tewarie, P., Hillebrand, A., Douw, L., van Dijk, B.W., Stufflebeam, S.M., Van Mieghem, P., 2016. A mapping between structural and functional brain networks. Brain Connect. 6, 298–311.
Meng, X.-L., Rubin, D.B., 1993. Maximum likelihood estimation via the ECM algorithm. Biometrika 80, 267–278.
Michie, P.T., Malmierca, M.S., Harms, L., Todd, J., 2016. The neurobiology of MMN and implications for schizophrenia. Biol. Psychol. 116, 90–97.
Näätänen, R., Alho, K., 1997. Mismatch negativity-the measure for central sound representation accuracy. Audiol. Neuro. Otol. 2, 341–353.
Oestreich, L.K.L., Whitford, T.J., Garrido, M.I., 2018. Prediction of speech sounds is facilitated by a functional fronto-temporal network. Front. Neural Circuits 12, 43.
Opitz, B., Rinne, T., Mecklinger, A., von Cramon, D.Y., Schroger, E., 2002. Differential contribution of frontal and temporal cortices to auditory change detection: fMRI and ERP results. Neuroimage 15, 167–174.
Osnes, B., Hugdahl, K., Specht, K., 2011. Effective connectivity analysis demonstrates involvement of premotor cortex during speech perception. Neuroimage 54, 2437–2445.
Penny, W.D., Stephan, K.E., Mechelli, A., Friston, K.J., 2004. Comparing dynamic causal models. Neuroimage 22, 1157–1172.
Rademacher, J., Morosan, P., Schormann, T., Schleicher, A., Werner, C., Freund, H.J., Zilles, K., 2001. Probabilistic mapping and volume measurement of human primary auditory cortex. Neuroimage 13, 669–683.
Rae, C.L., Hughes, L.E., Anderson, M.C., Rowe, J.B., 2015. The prefrontal cortex achieves inhibitory control by facilitating subcortical motor pathway connectivity. J. Neurosci. 35, 786–794.
Raffelt, D., Tournier, J.D., Rose, S., Ridgway, G.R., Henderson, R., Crozier, S., Salvado, O., Connelly, A., 2012. Apparent Fibre Density: a novel measure for the analysis of diffusion-weighted magnetic resonance images. Neuroimage 59, 3976–3994.
Ranlund, S., Adams, R.A., Díez, Á., Constante, M., Dutt, A., Hall, M.-H., Maestro Carbayo, A., McDonald, C., Petrella, S., Schulze, K., Shaikh, M., Walshe, M., Friston, K., Pinotsis, D., Bramon, E., 2016. Impaired prefrontal synaptic gain in people with psychosis and their relatives during the mismatch negativity. Hum. Brain Mapp. 37, 351–365.
Rigoux, L., Stephan, K.E., Friston, K.J., Daunizeau, J., 2014. Bayesian model selection for group studies - revisite. Neuroimage 84, 971–985.
Salisbury, D.F., Kuroki, N., Kasai, K., Shenton, M.E., McCarley, R.W., 2007. Progressive and interrelated functional and structural evidence of post-onset brain reduction in schizophrenia. Arch. Gen. Psychiatr. 64, 521–529.
Smith, R., Tournier, J.-D., Calamante, F., Connelly, A., 2012. Anatomically-constrained tractography: improved diffusion MRI streamlines tractography through effective use of anatomical information. Neuroimage 62, 1924–1938.
Smith, R.E., Tournier, J.D., Calamante, F., Connelly, A., 2013. SIFT: spherical-deconvolution informed filtering of tractograms. Neuroimage 67, 298–312.
Smith, R.E., Tournier, J.D., Calamante, F., Connelly, A., 2015. SIFT2: enabling dense quantitative assessment of brain white matter connectivity using streamlines tractography. Neuroimage 119, 338–351.
Smith, S.M., Jenkinson, M., Woolrich, M.W., Beckmann, C.F., Behrens, T.E.J., Johansen-Berg, H., Bannister, P.R., De Luca, M., Drobnjak, I., Flitney, D.E., Niazy, R.K., Saunders, J., Vickers, J., Zhang, Y., De Stefano, N., Brady, J.M., Matthews, P.M., 2004. Advances in functional and structural MR image analysis and implementation as FSL. Neuroimage 23, S208–S219.
Stephan, K.E., Penny, W.D., Daunizeau, J., Moran, R.J., Friston, K.J., 2009. Bayesian model selection for group studies. Neuroimage 46, 1004–1017.
Stephan, K.E., Penny, W.D., Moran, R.J., den Ouden, H.E.M., Daunizeau, J., Friston, K.J., 2010. Ten simple rules for dynamic causal modeling. Neuroimage 49, 3099–3109.
Sweet, L.H., 2011. N-back paradigm. In: Kreutzer, J.S., DeLuca, J., Caplan, B. (Eds.), Encyclopedia of Clinical Neuropsychology. Springer New York, New York, NY, pp. 1718–1719.
Tournier, J.D., Calamante, F., Connelly, A., 2012. MRtrix: diffusion tractography in crossing fiber regions. Int. J. Imaging Syst. Technol. 22, 53–66.
Wagner, G., De la Cruz, F., Schachtzabel, C., Güllmar, D., Schultz, C.C., Schlösser, R.G., Bär, K.-J., Koch, K., 2015. Structural and functional dysconnectivity of the fronto-thalamic system in schizophrenia: a DCM-DTI study. Cortex 66, 35–45.
Whitford, T.J., Mathalon, D.H., Shenton, M.E., Roach, B.J., Bammer, R., Adcock, R.A., Bouix, S., Kubicki, M., De Siebenthal, J., Rausch, A.C., Schneiderman, J.S., Ford, J.M., 2011. Electrophysiological and diffusion tensor imaging evidence of delayed corollary discharges in patients with schizophrenia. Psychol. Med. 41, 959–969.
Wigand, M., Kubicki, M., Clemm von Hohenberg, C., Leicht, G., Karch, S., Eckbo, R., Pelavin, P.E., Hawley, K., Rujescu, D., Bouix, S., Shenton, M.E., Mulert, C., 2015. Auditory verbal hallucinations and the interhemispheric auditory pathway in chronic schizophrenia. World J. Biol. Psychiatr. 16, 31–44.
Wirsich, J., Ridley, B., Besson, P., Jirsa, V., Benar, C., Ranjeva, J.P., Guye, M., 2017. Complementary contributions of concurrent EEG and fMRI connectivity for predicting structural connectivity. Neuroimage 161, 251–260.
Wright, D.K., Johnston, L.A., Kershaw, J., Ordidge, R., O'Brien, T.J., Shultz, S.R., 2017. Changes in apparent fiber density and track-weighted imaging metrics in white matter following experimental traumatic brain injury. J. Neurotrauma 34, 2109–2118.
Zhang, Y., Brady, M., Smith, S., 2001. Segmentation of brain MR images through a hidden Markov random field model and the expectation-maximization algorithm. IEEE Trans. Med. Imaging 20, 45–57.